Journal of African Earth Sciences 151 (2019) 315–323

Contents lists available at ScienceDirect

Journal of African Earth Sciences

journal homepage: www.elsevier.com/locate/jafrearsci

Rupture characteristics of a small-sized earthquake (M_W 4.2), onshore the south Red Sea, Saudi Arabia

Ali K. Abdelfattah[a,*], Sattam Almadani[a], Mohamad Fnais[a], Hussain J. Alfaifi[a], Nassir Al-Arifi[a], Abdullah Al-amri[a], Basem Al-Qadasi[a], Salvatore de Lorenzo[b]

[a] Department of Geology & Geophysics, College of Science, King Saud University, Riyadh, 11451, Saudi Arabia
[b] Dipartimento di Scienze della Terra, University di Bari "Aldo Moro", Via Orabona 4, I-70125, Bari, Italy

ARTICLE INFO

Keywords:
Empirical Green's function
Small-sized earthquake
Rupture characteristics
Jizan
Saudi Arabia
Waveform inversion

ABSTRACT

The present study is based on the use of Empirical Green's Function (EGF) deconvolution technique to retrieve the slip distribution of the 2014 M_w 4.2 Jizan earthquake, Saudi Arabia. Two datasets of complex Source Time Functions (STFs) were retrieved using two appropriate EGF events. We inverted the STF datasets to recover the slip distribution over both nodal planes, using the Bayesian modeling followed by a linear least-squares method. The inversion was performed assuming both planes as the fault plane and examined the goodness of fit for each nodal plane. Based on a series of finite-source inversions using different rupture velocities, we resolved the rupture velocity at 2.7–2.8 km/s and the fault plane of NNW trending; paralleling the Red Sea rift. Using the estimated rupture velocities and the preferred fault plane, we imaged quite similar slip models, exhibiting two slip patches located to the updip and downdip directions from the hypocentre. The spatiotemporal slip distributions revealed a complex rupture history of such small-sized earthquake is likely to that reported for large-sized earthquakes. A seismic moment of 2.8–3.2E+15 NM and a corresponding moment magnitude of 4.2-4-3 are inferred. The stress drops obtained from the slip distribution models were 2.2–2.5 MPa; indicating a typical value that characterized the plate-boundary earthquakes.

1. Introduction

The study of rupture characteristics of small-sized earthquakes can provide interesting observations to improve our understanding of geodynamic processes in the in the vicinity of an active rift system. The source time functions (STFs) are used to investigate the rupture propagation of small-to-moderate-sized earthquakes. Along the rupture propagation direction, the STFs have large amplitudes and short durations; along the direction opposite to that of rupture propagation, the STFs have small amplitudes and long durations. One of the methods that are commonly used to retrieve the STFs for small-to-moderate size earthquakes is the Empirical Green's Function (EGF) deconvolution technique (Li and Thurber, 1988; Mori and Frankel, 1990; Mueller, 1985; Zollo et al., 1995; Courboulex et al., 1996; Fletcher and Spudich, 1998; Abercrombie et al., 2001; Abdel-Fattah and Badawy, 2002). The method was firstly introduced by Hartzell (1978). Often source studies based on Empirical Green Functions (EGFs) are used to recover point-source characteristics with a complex STFs and their extension to a finite rupture inversion are not straightforward. The inversion of STFs, based on the finite-source model assumption, was applied for small-sized earthquakes and induced microearthquakes (Mori and Hartzell, 1990; Mori, 1993; Ide, 2000; Abdel-Fattah, 2002; Abdel-Fattah et al., 2014; Yamada et al., 2005; de Lorenzo et al., 2008).

The seismic activity in the Arabian Shield, the eastern flank of the Red Sea, is presumably influenced by a complex geodynamic process that coupled the rifting system, in the Red Sea, with upwelling magma of shallow asthenosphere beneath the shield (Abdel Fattah et al., 2017). On 23 January 2014, a small-sized earthquake of Mw 4.4 occurred in the upper crust of Jizan province, the coastal plain of the Red Sea, Southwest Saudi Arabia (Fig. 1). The event caused minimal local damage, but it was widely felt in V to VI in the epicenter area based on the modified Mercalli intensity scale (El-Hadidy, 2015). The aftershock distribution and the moment tensor solution implied dextral strike-slip displacements along the ENE (Abdel Fattah et al., 2017). The epicenter area that belongs to the western Saudi Arabia continental flank, extends along the eastern coastlines of the Red Sea, is geologically enriched with Cenozoic basaltic fields, numerous fault trends, and magmatic intrusions, causing crustal heterogeneities associated with asperities and barriers. The recordings of the Broadband seismic stations, that operated by the Saudi Geological Survey (SGS), with good azimuth

* Corresponding author.
E-mail addresses: ali_kamel100@yahoo.co.uk, ali_kamel@yahoo.com (A.K. Abdelfattah).

https://doi.org/10.1016/j.jafrearsci.2018.12.014
Received 24 September 2018; Received in revised form 21 October 2018; Accepted 12 December 2018
Available online 13 December 2018
1464-343X/

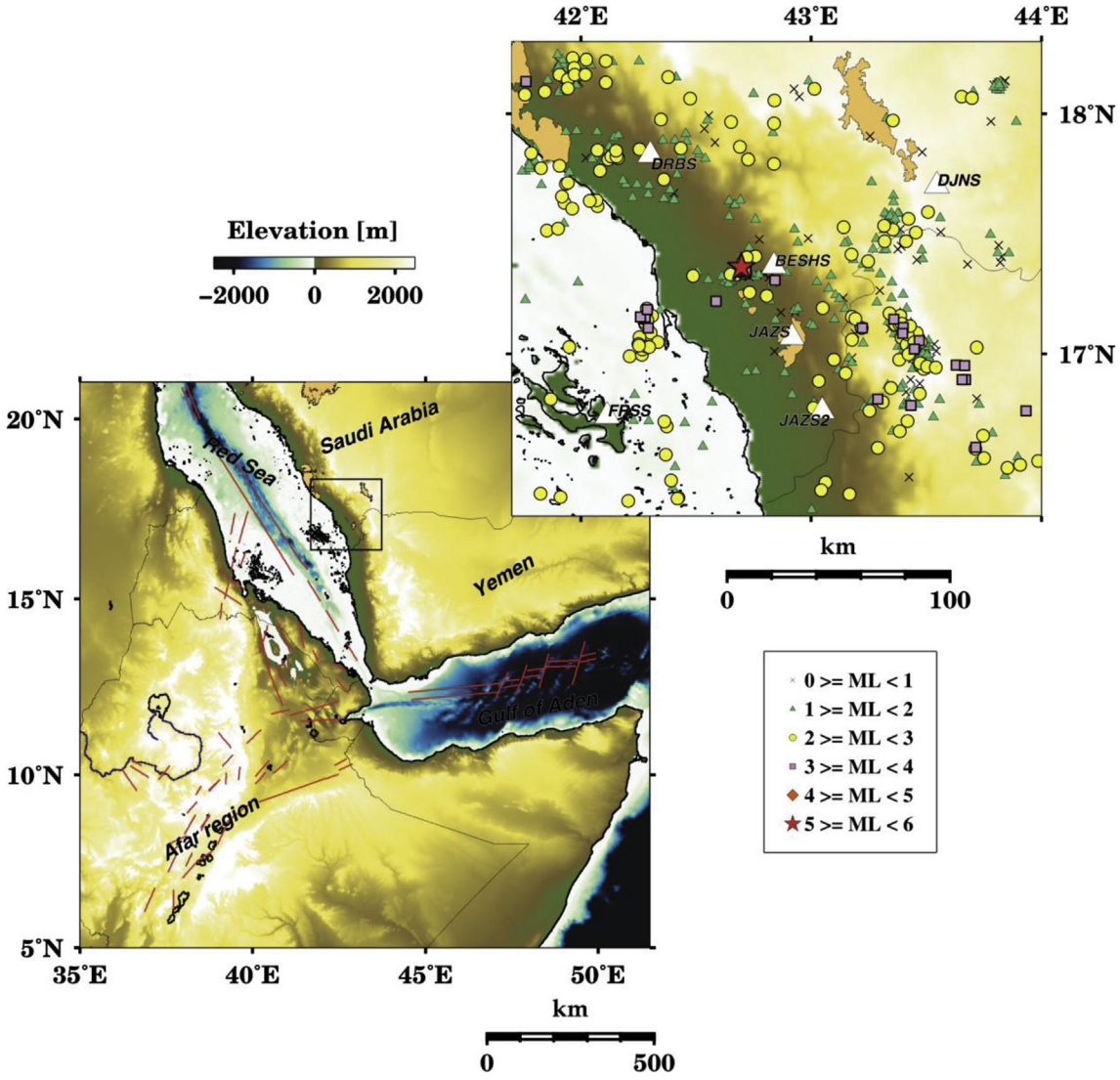

Fig. 1. (a) Map showing the tectonic plate boundary in the vicinity of the studied area. The square at the south shores of the Red Sea near the Yemen-KSA border shows the area of interest. (b) Map showing the spatial distribution of epicentres in the study area within the time period 2007–2014 and the spatial locations of the seismic stations used in this analysis (open white-triangles).

coverage, provided an impetus to examine the rupture model of such small-sized earthquake. The stations are equipped with three-component Trillium velocity seismometers having a flat response spectrum in the range of 0.02–120 s. The analog records are digitized by 24-bit A/D at a sampling rate of 50 Hz. Fig. 1 shows the station distribution used in the present study and the spatial distribution of the mainshock epicenter.

Few studies have examined the spatial distributions of fault slip for small events that required adequate waveform data are required. High quality seismograms, from the local seismic network of Saudi Arabia, give a good opportunity to capture high frequency (> 1 Hz) waves in order to explore the source process of the 2014 Jizan earthquake. We characterized the rupture propagation of such small-sized event using a technique based on the use of the empirical Green's function (EGF) deconvolution technique to retrieve the STFs which are then inverted to obtain the spatiotemporal slip distribution over the fault plane. The current analysis is carried out to resolve the fault plane, rupture velocity, focal depth and stress drops. In the region where the large earthquakes infrequently occur, the analysis of such an event is very important for seismic hazard assessment.

2. Tectonic settings

The geodynamic process nearby the epicenter area, illustrated by the inset square in Fig. 1, is attributed to the complex triple junction of active spreading ridges along the Red Sea, Gulf of Aden, and East African Rift Zone. The figure is also shown the spatial distribution of epicentres in the study area within the time period 2007–2014. The epicenter area, as a part of the Arabian Shield, is characterized by the presence of dike intrusions and two main systems of normal NW-SE faults and NNW-SSE strike-slip faults called Najd Fault system (NFS) of sinistral strike-slip movement (Abdel Fattah et al., 2017). The NW–SE faults in the Red Sea rift system are conjugated by transform faults that represent the Precambrian Pan-African structures of dextral strike-slip displacement striking in an ENE–WSW direction (Al Ganad et al., 1994; Beydoun et al., 1998; Johnson, 1998; Vita-Finzi, 2001; Fournier et al., 2007).

3. Hypocenter relocations

We applied the double-difference technique of Waldhauser and Ellsworth (2000) to improve the precise locations of Abdel Fattah et al. (2017) for a total number of 85 earthquakes using the singular value

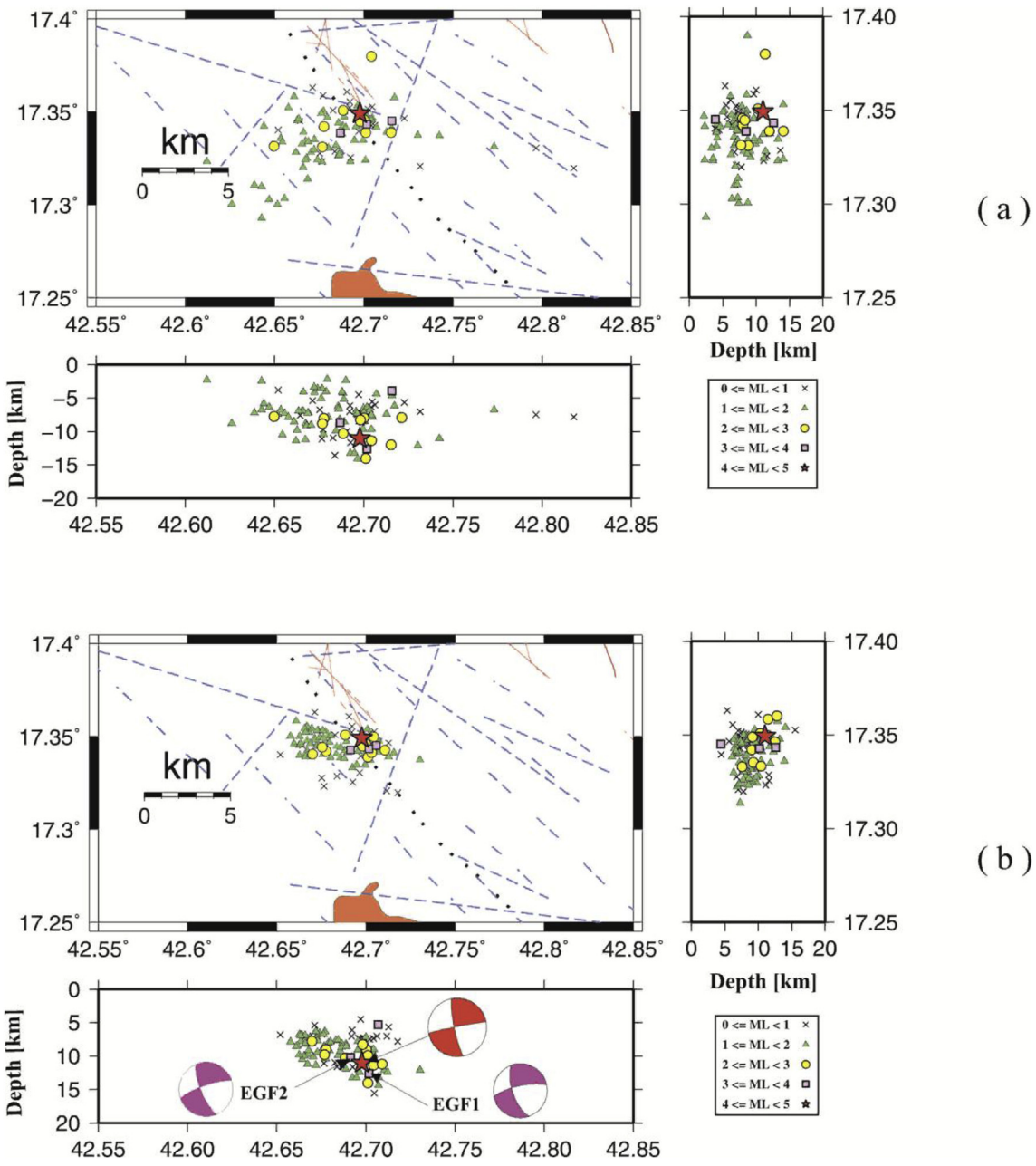

Fig. 2. Map showing the spatial distribution of aftershocks and the mainshock (red star) (a) absolute location and (b) relative location techniques, respectively. The right panels show the distribution of hypocenters along the latitude and the bottom panels show the distribution of hypocenters along the longitude. Different symbols correspond to different magnitude ranges of aftershocks. The focal mechanisms of the mainshock (red beach ball) and two aftershocks used as EGF events (purple beach ball) are shown. (For interpretation of the references to colour in this figure legend, the reader is referred to the Web version of this article.)

decomposition (SVD) method. The differential travel times of P- and S-waves were measured using both the absolute location and waveform cross-correlation. The cross-correlation was performed in the time domain using a time window centered on both P- and S- waves. Time series of 1 s and 2 s lengths were used to separately include the P- and S-waves recorded by the vertical and horizontal components, respectively. To reduce the low- and high-frequency noises, the waveform data were filtered using a second-order Butterworth Band-pass filter with a frequency band from 1 to 4 Hz. A total number of 1159 P and 683 S arrivals that exhibited correlation coefficients greater than 0.70 were used to relocate the events. The hypoDD and waveform cross correlation analysis were used to improve hypocentre locations of Abdel Fattah et al. (2017) and choose appropriate EGFs. Fig. 2a&b show absolute and relative locations, respectively. Taking into considerations the relocation uncertainties, the epicentre locations were spatially scattered to the west direction from the mainshock. However, the majority of hypocentres along the longitude were slightly aligned to the NW direction. Most aftershocks are located upwards to the mainshock hypocentre with focal depths shallower than 10 km. The 1-D velocity model of Rodgers et al. (1999) was used in the analysis.

4. Relative source time functions

The resolution of STFs retrieved from the EGF deconvolution technique depends on the quality of the available data and their azimuth coverage. The small event of similar location and focal mechanism that is used as EGF events should have smaller rupture duration to be representative of the Green's function. To keep a good signal-to-noise

Table 1
Hypocentre and fault plane parameters of the mainshock and EGF events used in the present analysis.

ID	O.T.	Lat. [°]	Long. [°]	Depth [km]	Mw	Strike [°]	Dip [°]	Rake [°]
M	20140123 150036.59	17.3493	42.6977	11.2	4.3	259	87	−171
EGF1	20140125 002813.04	17.3433	42.7017	12.6	3.3	251	78	−164
EGF2	20140126 122626.73	17.3427	42.6913	10.2	3.1	257	75	−156

M denotes the mainshock and EGF1 and EGF2 denote the empirical Green's function events.

ratio, an adequate magnitude of at least one order of magnitude less than that of the mainshock is required. In this study, we could select only two aftershocks of a magnitude greater than 3.0 that are appropriate to be used as EGF events. The hypocentral parameters of the EGF events and mainshock are listed in Table 1. Fig. 2 shows the relative locations of the mainshock and the EGF events.

The deconvolution was performed in the time-domain by the non-negative least-square (NNLS) algorithm of positive constraints (Lawson and Hanson, 1974). Using vertical components, the STFs were separately deconvolved using P waves. When the P waves were not clear, the clear enough S waves recorded on the transverse or radial components were separately used. An example of the deconvolution procedure to get the relative STFs is shown in Fig. 3 that demonstrates the waveform of the target event (black), the waveform of the kernel event (blue), both synchronized and aligned. In addition, the figure shows the synthetic waveform of the target event (red) and the relative source time functions (green). Along with the deconvolved STFs, the velocity records of both the EGF and the mainshock are shown in Fig. 3; exhibiting complex STFs. The variations of STFs against the azimuths and hypocenter distances revealed rupture directivity along the strike and dip directions (Fig. 4). The dipward directivity might explain why the retrieved STFs at the JAZS and JAZS2 stations have some differences, although the station azimuths are similar (difference less than 10°). The nodal plane striking ENE-WSW is aligned along the stations DJNS and FRSS. The STFs at DJNS and FRSS are similar to some extent, while on the contrary, the STFs at DRBS and JAZS are clearly differ, supporting the NNW trending plane, as the fault plane, and if directivity is associated with this event, this is towards DRBS. Moreover, the STFs at stations JAZS and JAZS2 show two peaks, supporting radiation complexity.

5. Slip distribution models

Following the linear inversion technique of Ide et al. (1996) based on the Bayesian modeling, we inverted the STF datasets to retrieve the spatiotemporal distribution of slip along both nodal planes. The focal mechanism is assumed to be fixed during the inversion course. The spatiotemporal smoothing was applied, to stabilize the inversion. Using Akaike's Bayesian information criterion (Akaike, 1980) the Laplacian of the total slip distribution and the first order derivative of the slip-rate were minimized by spatial and temporal smoothing constraints, respectively. Thus, the model parameters were recovered using the NNLS. During the inversion scheme, the rupture is circularly expanded with a constant rupture velocity by triangular functions of equal distance intervals distributed over the possible fault plane (strike and dip) and time. An adequate dimension, of the fault plane of $2.0 \times 2.0\,km^2$, was

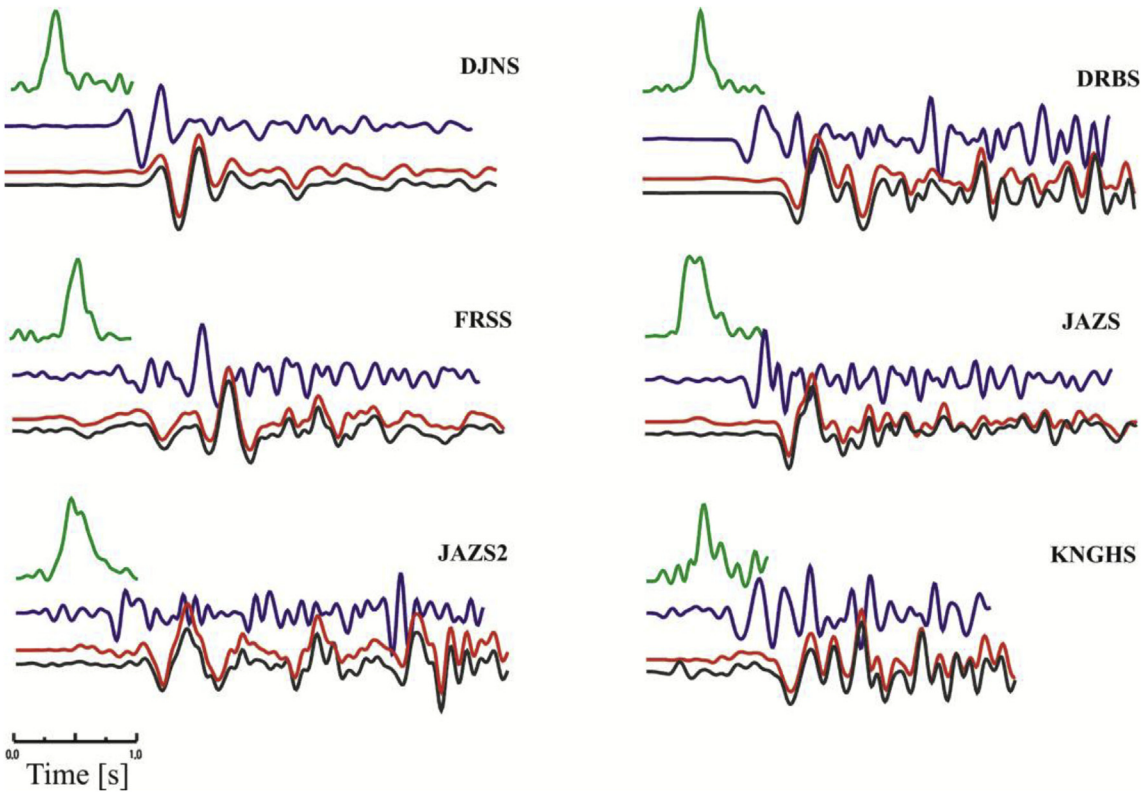

Fig. 3. Plot showing an example to retrieve the STFs (green lines) by an iterative time-domain deconvolution technique that used to remove the structure effects. The plot shows the waveform of the target event (black lines), the waveform of the selected EGF event (blue lines), both synchronized and aligned, and the synthetic waveform (red lines) as the result of the convolution of the waveform of the EGF event (blue lines) and the retrieved STFs (green lines). The station's name was written close to its relative time series. (For interpretation of the references to colour in this figure legend, the reader is referred to the Web version of this article.)

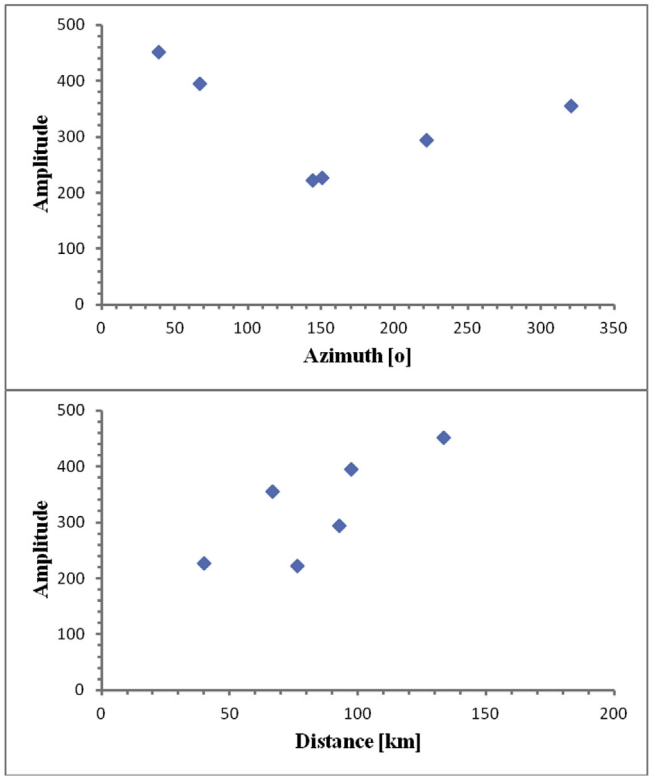

Fig. 4. The variation in amplitudes of the retrieved STFs against the (a) station azimuths and (b) station distances.

assumed to allow the slip distributions in all direction starting from the hypocenter. Before the inversion course, the retrieved STFs were filtered by a six-order Butterworth low-pass filter with a corner frequency of 10 HZ to minimize the high-frequency noise due to the deconvolution artifacts. A series of inversions using different rupture velocities and focal depths was first performed to resolve the best-fit rupture velocity and focal depth, based on the use of an appropriate duration of the source-time function that is directly proportional to the ratio between the rupture velocity and the shear wave velocity assumed equal to 3.6 km/s, as taken from Rodgers et al. (1999). Several inversion tests were carried out, varying the rupture velocity with a step of 0.2 km/s

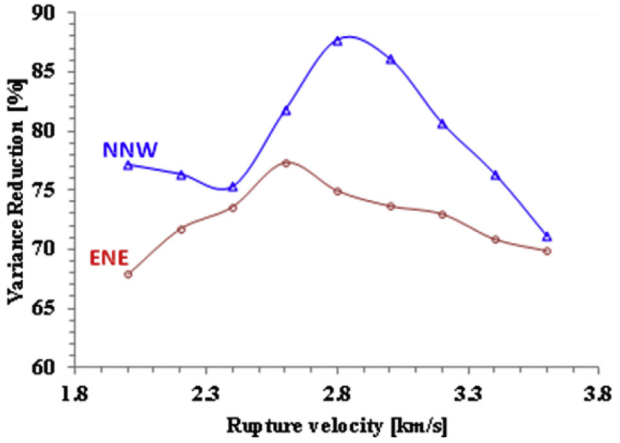

Fig. 6. Plot showing the goodness of fit (Variance Reduction) versus the rupture velocities for each nodal plane (NNW and ENE).

and the focal depth with a step of 1 km, obtaining the maximum variance reduction at a rupture velocity of 2.7 ± 0.3–2.8 ± 0.2 km/s and a focal depth of 11.6 ± 0.5–10.8 ± 0.9 km using EGF1 and EGF2, respectively, as shown in Fig. 5. The inversions were performed assuming both nodal planes as the fault plane and we examine the goodness of fit (Variance Reduction) for each nodal plane, see Fig. 6. The Variance Reduction shows significantly larger values for the NNW trending plane. The slip models were then retrieved along the NNW fault trend using the best fit rupture velocities and focal depths along a grid of subfaults of 0.1 × 0.1 km^2 and rupture duration of 0.28 s of nine triangle functions over each subevent to adjust the slip to be expanded spatially and temporally with smoothing constraints along the fault plane.

Fig. 6 shows the obtained slip distribution models and the time sequences of snapshots estimated over the NW fault plane with a strike ϕ = 148° and a dip δ = 83°, as determined by Abdel Fattah et al. (2017). The synthetic seismograms obtained from the two slip distribution models are shown in Fig. 7. The slip models revealed quit similar patterns of two different sizes of asperities; the overall pattern exhibits elongated distribution along the dip directions. Two slip patches were located updip and downdip from the hypocentre, respectively. The slip models showed a maximum slip value of about 0.4 m–0.45 m for upward and downward slip patches, respectively. The

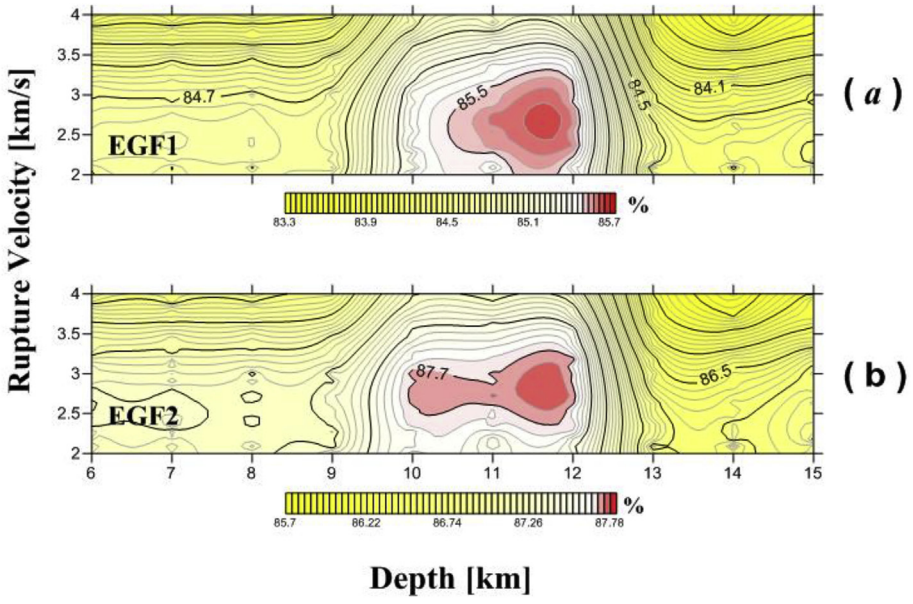

Fig. 5. The grid search method over different focal depths and rupture velocities as a function of variance reduction. Results represent the inversion tests of different rupture velocities of 0.2 km/s increment and focal depths of 1 km increment, obtaining the maximum variance reduction at rupture velocity of 2.7 ± 0.3–2.8 ± 0.2 km/s and focal depth of 11.6 ± 0.5–10.8 ± 0.9 km using (*a*) EGF1 and (b) EGF2, respectively.

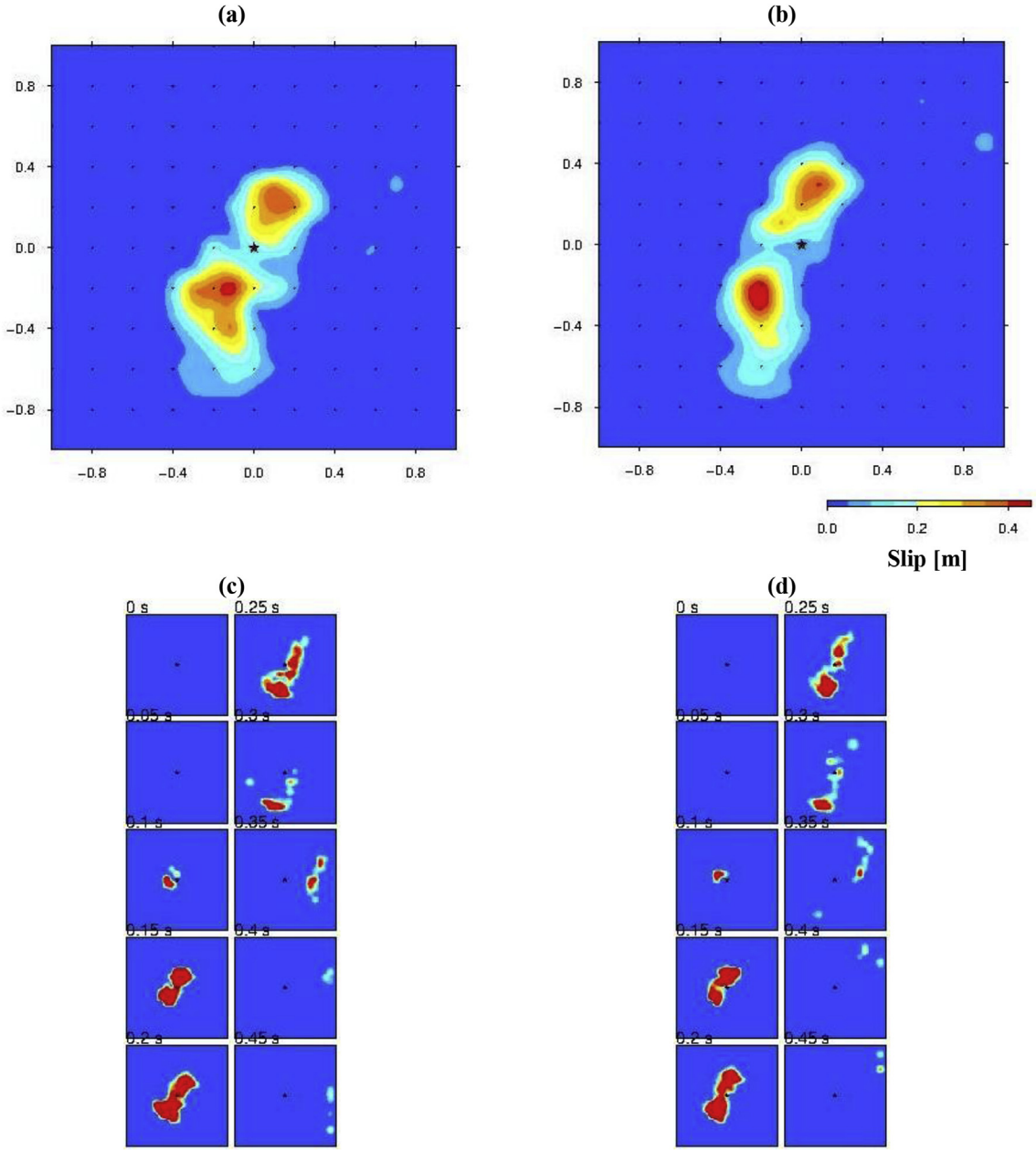

Fig. 7. Plot showing the best slip distribution models that retrieved along the NNW fault plane (a) at a focal depth of 10.8 km and rupture velocity of 2.8 km/s using the EGF1 and (b) (a) at a focal depth of 11.6 km and rupture velocity of 2.7 km/s using the EGF2. The plots (c) and (d) represent the time sequences of snapshots retrieved using the waveform data of the EGF1 and the EGF2, respectively.

time sequences of snapshots, as shown in Fig. 7c and d, show complex rupture models. At the early stage, the rupture initiated with two small slip points upward and downward along the dip direction around the hypocentre. Rupture expands along rupture fronts having an approximately circular shape. Subsequently, the rupture propagates unilaterally downward from the hypocentre until the rupture stops towards the ENE direction. Fig. 8a and b shows the comparison between the observed and synthetic source time functions computed from the resulting rupture models in Fig. 7a and b.

The resulting rupture models release seismic moment of 2.8–3.2E +15 Nm and moment magnitude of 4.2–4.3. The seismic potency ranged from 9.3 to 10.6E + 4 m^3. The moment magnitudes inferred in this study is somewhat smaller than that estimated by Abdel Fattah et al. (2017) using moment tensor inversion based on the assumption of a point source, which is 4.4. As a matter of fact, the seismic moment obtained in this study is dependent on the accuracy of moment magnitude estimated for the EGF events, which determined by Abdel Fattah et al. (2017) to be as 3.3 and 3.1 for EGF1 and EGF2, respectively. Using the relation of Kanamori and Anderson (1975), the static stress drops were estimated to be 2.2–2.5 Mpa along the rupture length of 1.08 km with averaged slip value of 7.9–9.1 cm. The rigidity was assumed to be 30 Gpa.

6. Discussions

This study provides interesting observations that can improve our understanding of seismicity processes in the vicinity of an active rift system likes the Red Sea rifting system. We investigate the rupture model of the 2014 Jizan earthquake using the approach that combined the decomposition of the structure effects by using empirical Green's functions (EGF) and modeling of the reconstructed RSTFs with slip distributions along one of the possible focal planes. The preliminary

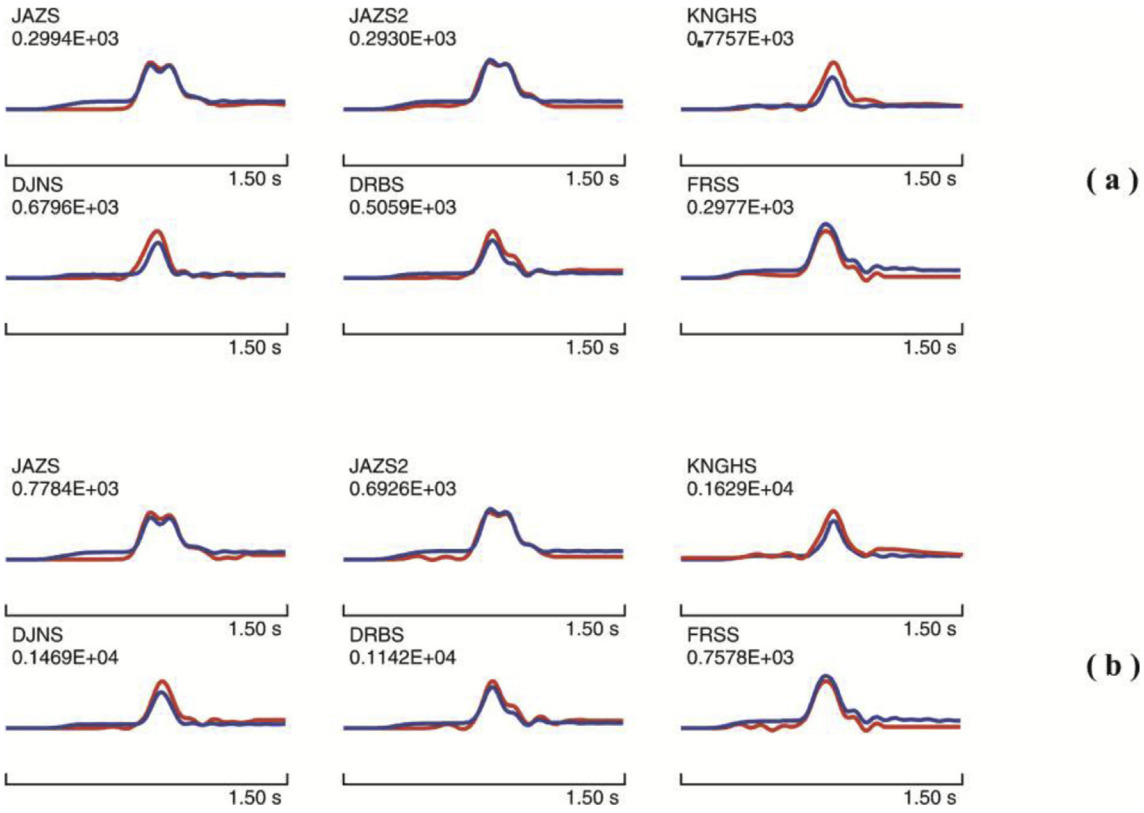

Fig. 8. Comparison between the retrieved STFs (red solid lines) and their synthetic waveforms (blue solid lines) that calculated from the resultant slip distribution models in Fig. 6 (a) for a focal depth of 11.6 ± 0.5 km and rupture velocity of 2.7 ± 0.3 km/s using the EGF1 and (b) for a focal depth of 10.8 ± 0.9 km and rupture velocity of 2.8 ± 0.2 km/s using the EGF2. The retrieved STFs were filtered by a six-order Butterworth low-path filter having a corner frequency of 10 Hz. (For interpretation of the references to colour in this figure legend, the reader is referred to the Web version of this article.)

analysis showed that the variation in amplitudes and pulse durations exhibits complex rupture behavior along the azimuth and the distance. The resulting slip distribution models along the NNW striking plane imply a complex rupture model. The rupture elongates outward the hypocentre along the dip direction and exhibits two slip patches in the downdip and the updip direction. It is worth stressing that similar slip distribution models of downward rupture directivities were imaged for moderate-sized earthquakes in Aegean region (Baumont et al., 2002; Roumelioti et al., 2003) and for small-sized earthquakes in South Korea (Abdel-Fattah et al., 2014).

For such a small event, whose mechanism is strike slip along nearly vertical planes, it is difficult to identify the fault plane. Both nodal planes can be plausible in the area, from a tectonic point of view. From the STFs it seems more probable that the NNW striking plane as the fault plane as inferred from the obtained rupture models. From a tectonic point of view, the preferred fault plane is in consistence with the regional faults originated from the dominant extensional-stress regime in the region. The Arabian shield has influenced by several orogenic events. First, the Pan-African orogeny initiated due to the extensional stresses African and Arabian shields, which followed by upwelling magmas associated with magmatic intrusions. The last stage of tectonic deformation event in the region is called the Najd Fault Systems, which generates pull-apart basins rejuvenated with extensive magmatic activities during the Oligocene to the present. These orogenic events are manifested in the Arabian Shield by three prominent systems of dextral NE to ENE strike-slip faults, normal NW faults, and sinistral NNW strike-slip faults (Al Ganad et al., 1994; Beydoun et al., 1998; Johnson, 1998; Vita-Finzi, 2001; Fournier et al., 2007); where seismic activities occur. The NNW failure plane is speculated reactivation of high-angle pre-existing faults that represented the Pan-African fault systems (Greenwood et al., 1980) in the Precambrian basement of the epicenter area.

One of the most fundamental parameters that can improve our understanding of peculiar seismicity processes, in the vicinity of an active rift system, is the stress drop. It is noteworthy that the low stress drops that characterized shallow earthquakes are presumably attributed to poor mechanical properties of the layers accommodated in the crust (Tusa et al., 2006). Moreover, estimates of stress drops for small to moderate-sized earthquakes are often based on the assumption of a circular source model (Brune, 1970, 1971; Madariaga, 1976). In the present study, we could not investigate the source scaling relations of the sequence because the limited magnitude ranges of the sequence and the band limited data of the SGS recording system (100 samples/s). However, the previous studies revealed that the seismic activity regions in the vicinity of the area of interest characterized by low stress drops and shallow earthquakes. In the Arabian Shield, north to the analyzed earthquake, the 2009 Al-Ays earthquake sequence released low stress drops of 1.0–3.7 MPa (Abdel-Fattah et al., 2014). In the Red Sea region, the average stress drop is 8.2 ± 7.8 for south Red Sea (Hofstetter and Beyth, 2003), 1.2 ± 0.97 for Afar region (Kebede and Kulhanek, 1989), 3.1 ± 0.31 MPa for Suez-Cairo Shear Zone of Egypt (Abu Elenean et al., 2010), and in the range of 1.2–3.2 MPa for the Gulf of Aqaba (Pinar and Turkelli, 1997; Abdel-Fattah et al., 2006; Allmann and Shearer, 2009). In the Gulf of Suez, the 2001 earthquake swarm at Shadwan Island, the stress drops are ranged between 0.04 and 1.0 MPa (Badawy and Abdel-Fattah, 2001). On a global scale, the study of Allmann and Shearer (2009) exhibited a strong evidence for earthquake self-similarity over 13 orders of magnitude, indicating apparently variation with stress regime. The stress drop that obtained from this study has a typical value for a plate-boundary earthquake (Ruff, 2002), implying that the earthquake may attribute to the active tectonic processes acting in the Red Sea rifting system. Our estimate of stress drop is

consistent with the results of Archuleta et al. (1982), Mori and Frankel (1990), and Tajima and Tajima (2007) for earthquakes of Mw ~ 4.0. The low stress drop of small-sized earthquakes reflects that the crust is characterized by brittleness and proneness to high strain accumulation due to the presence of barriers and asperities that control the rupture process of earthquakes in the fault zone. It is noteworthy that the upper crust of the area of interest is characterized by the roughness magmatic intrusions, which emphasize the presence of barriers and asperities. Moreover, the obtained slip distribution models and the aftershock distribution to the west of the mainshock location revealed a redistribution of stress accumulation mechanism triggered by the mainshock rupture in the dislocation zone. In short, despite of the 2014 Jizan earthquake is a small magnitude event, the present analysis exhibits seismic characteristics similar to that reported for large-size earthquakes.

7. Conclusions

In this study a small magnitude earthquake in Saudi Arabia was analyzed. The detailed analysis was preformed through the double difference technique to improve the locations of the aftershock sequence, the deconvolution technique of Empirical Green's Functions to obtain relative moment rate functions, and subsequently to invert them in order to calculate the slip distribution on the fault plane. The refinement relocation using double difference technique revealed that the aftershock distributions were not aligned a clear trend with respect to the mainshock. The fault geometry, rupture velocity, and stress drops were resolved from the retrieved slip distribution model. The slip distribution model of the 2014 earthquake provides an evidence of complex source process of moderate size earthquake similar to that reported for large-sized earthquakes. The rupture velocity at 2.7–2.8 km/s was resolved along the nodal plane striking NNW that is the more likely fault plane of a sinistral strike-slip motion; implying a rejuvenation of pre-existing faults related to the Pan-African fault system. The slip models exhibited a complex rupture history of two slip patches located to the updip and downdip directions from the hypocentre. A seismic moment of 2.8–3.2E + 15 NM and a corresponding moment magnitude of 4.2-4-3 are inferred. The stress drops obtained from the slip distribution models were 2.2–2.5 MPa; indicating a typical value that characterized the plate-boundary earthquakes. The study provides informative results that can be used to improve the seismic hazard assessment in the region.

Acknowledgments

We are grateful to the Saudi Geological Survey (SGS) for providing the broadband seismic data. The authors would like to extend their sincere appreciation to the Deanship of Scientific Research at King Saud University for funding this Research group no. (RG-1437-010). Generic Mapping Tools developed by Wessel and Smith (1991) was used for most data mapping.

Appendix A. Supplementary data

Supplementary data to this article can be found online at https://doi.org/10.1016/j.jafrearsci.2018.12.014.

References

Abdel Fattah, A.K., Hussein, H.M., El Hady, S., 2006. Another look at the 1993 and 1995 Gulf of Aqaba earthquake from the analysis of teleseismic waveforms. Acta Geophys. 54 (3), 260–279.
Abdel-Fattah, A.K., 2002. Source characteristics of a moderate earthquake (M 4.9) using the empirical Green's function technique. Ann. Geophys. 45 (5), 575–586.
Abdel-Fattah, A.K., Badawy, A., 2002. Source process of the southeast Beni-Suef, northern Egypt earthquake using empirical Green's function technique. J. Seismol. 6 (2), 153–161.
Abdel-Fattah, A.K., Kim, K., Fnais, M., Al-Amri, A., 2014. Source process and tectonic implication of the January 20, 2007 Odaesan earthquake, South Korea. PEPI 229, 72–81.
Abdel-Fattah, A.K., Al-Amri, A., Abd el-aal, A., Zaidi, F.K., Fnais, M., Almadani, S., Al-Arifi, N., 2017. The 23 January 2014 Jizan earthquake and its tectonic implications in southwestern Saudi Arabia. Tectonophysics 712–713, 494–502.
Abercrombie, R.E., Antolik, M., Felzer, K., Ekström, G., 2001. The 1994 Java tsunami earthquake: slip over a subducting seamount. JGR 106, 6595–6607.
Abou Elenean, K.M., Mohamed, A.M., Hussein, H.M., 2010. Source parameters and ground motion of the Suez-Cairo shear zone earthquakes, Eastern Desert, Egypt. Nat. Hazards 52, 431–451.
Akaike, H., 1980. Likelihood and Bayes procedure. In: Bernardo, J.M. (Ed.), Bayesian Statistics. University Press, Valencia, Spain, pp. 143–166.
Al Ganad, I., Lagny, P., Lescuyer, J., Ramboz, C., Touray, J., 1994. Jabali, a Zn-Pb-(Ag) carbonate-hosted deposit associated with Late Jurassic rifting in Yemen. Miner. Deposita 29 (1), 44–56.
Allmann, B.P., Shearer, P.M., 2009. Global variations of stress drop for moderate to large earthquakes. JGR 114. https://doi.org/10.1029/2008JB005821.
Archuleta, R.J., Cranswick, E.C., Mueller, C., Spudich, P., 1982. Source parameters of the 1980 Mammoth Lakes, California, earthquake sequence. JGR 87, 4595–4607.
Badawy, A., Abdel-Fattah, A.K., 2001. August earthquake swarm at Shadwan Island, Gulf of Suez, Egypt. GJI 167 (1), 288–296.
Baumont, D., Courboulex, F., Scotti, O., Melis, N.S., Stavrakakis, G., 2002. Slip distribution of the M_w 5.9, 1999 Athens earthquake inverted from regional seismological data. GRL 29 (15). https://doi.org/10.1029/2001GL014261.
Beydoun, Z., As-Saruri, M., El-Nakhal, H., Al-Ganad, I., Baraba, R., Nani, A., Al-Aawah, M., 1998. International lexicon of stratigraphy, Republic of Yemen. pp. 3.
Brune, J., 1970. Tectonic stress and spectra of seismic shear waves from earthquakes. JGR 75, 4997–5009.
Brune, J.N., 1971. Correction. J. Geophys. Res. 76, 5002.
Courboulex, F., Virieux, J., Deschamps, A., Gibert, D., Zollo, A., 1996. Source investigation of a small event using empirical Green's functions and simulated annealing. GJI 125, 768–780.
de Lorenzo, S., Filippucci, M., Boschi, E., 2008. An EGF technique to infer the rupture velocity history of a small magnitude earthquake. JGR 113. https://doi.org/10.1029/2007JB005496.
El-Hadidy, S., 2015. Seismicity and seismotectonic setting of the Red Sea and adjacent areas. In: Rasual, N.M.A., Stewart, I.C.F. (Eds.), The Red Sea: the Formation, Morphology, Oceanography and Environment of a Young Ocean Basin. Springer, London, pp. 151–159.
Fletcher, J.B., Spudich, P., 1998. Rupture characteristics of the three M 4.7 (1992-1994) Parkfield earthquakes. JGR 103, 835–854.
Fournier, M., Huchon, P., Khanbari, K., Leroy, S., 2007. Asymmetry and segmentation of passive margin in Socotra, Eastern Gulf of Aden, controlled by detachment faults? Geochem. Geophys. Geosyst. 8 (3) Q03013 (03010.01029/02006G001318).
Greenwood, W.R., Anderson, R.E., Fleck, R.J., Roberts, R.J., 1980. Precambrian geology history and plate tectonic evolution of the Arabian shield. Saudi Arabia Direct. General Mineral Resourc. Bull. 24, 1–35.
Hartzell, S.H., 1978. Earthquake aftershocks as Green's functions. GRL 5, 1–4.
Hofstetter, R., Beyth, M., 2003. The Afar Depression: interpretation of the 1960–2000 earthquakes. GJI 155, 715–732.
Ide, S., 2000. Complex source processes and the interaction of moderate earthquakes during the earthquake swarm in the Hida-Mountains, Japan, 1998. Tectonophysics 334, 35–54.
Ide, S., Takeo, M., Yoshida, Y., 1996. Source process of the 1995 Kobe earthquake: determination of spatio-temporal slip distribution by Bayesian modelling. BSSA 86, 547–566.
Johnson, P.R., 1998. Tectonic Map of Saudi Arabia and Adjacent Areas. Deputy Ministry for Mineral Resources. USGS TR-98-3, Saudi Arabia.
Kanamori, H., Anderson, D., 1975. Theoretical basis of some empirical relations in seismology. BSSA 65 (5), 1073–1095.
Kebede, F., Kulhánek, O., 1989. Source parameters of selected earthquakes on the central and western margin of Afar. Tectonophysics 170, 243–257.
Lawson, C.L., Hanson, R.J., 1974. Linear Least Squares with Linear Inequality Constraints, Solving Least Squares Problems. Prentice-Hall, Englewood Cliffs (NJ), pp. 161.
Li, Y., Thurber, C.H., 1988. Source properties of two microearthquakes in Kilauea volcano, Hawaii. BSSA 78, 1123–1132.
Madariaga, R., 1976. Dynamics of an expanding circular fault. BSSA 66 (3), 639–666.
Mori, J., 1993. Fault plane determinations for three small earthquakes along San Jacinto fault California: search for cross faults. JGR 98, 17711–17722.
Mori, J., Frankel, A., 1990. Source parameters of aftershocks of the 1986 north Palm Springs earthquake. BSSA 80, 278–295.
Mori, J., Hartzell, S., 1990. Source inversion of the 1988 Upland, California, earthquake: determination of a fault plane for a small event. BSSA 80, 507–517.
Mueller, C., 1985. Source pulse enhancement by deconvolution of an empirical Green's function. GRL 12, 33–36.
Pinar, A., Turkelli, N., 1997. Source inversion of the 1993 and 1995 Gulf of Aqaba earthquakes. Tectonophysics 293, 279–288.
Rodgers, A., Walter, W., Mellors, R., Al-Amri, A., Zhang, Y., 1999. Lithospheric structure of the Arabian Shield and Platform from complete regional waveform modelling and surface wave group velocities. GJI 138, 871–878.
Roumelioti, Z., Dreger, D., Kiratzi, A., Theodoulidis, N., 2003. Slip distribution of the 7 September 1999 Athens earthquake inferred from an empirical Green's function study. BSSA 93 (2), 775–782.
Ruff, L.J., 2002. State of stress within the earth. In: Lee, W.H.K. (Ed.), International Handbook of Earthquake & Engineering Seismology (Part A). Academic Press,

London, pp. 539–558.
Tajima, R., Tajima, F., 2007. Seismic scaling relations and aftershock activity from the sequences of the 2004 mid Niigata and the 2005 west off Fukuoka earthquakes (Mw 6.6) in Japan. JGR 112. https://doi.org/10.1029/2007JB004941.
Tusa, G., Brancato, A., Gresta, S., Malone, S.D., 2006. Source parameters of micro-earthquakes at Mount St. Helens (USA). Geophys. J. Int 166, 1193–1223.
Vita-Finzi, C., 2001. Neotectonics at the Arabian plate margins. J. Struct. Geol. 23 (2), 521–530.
Waldhauser, F., Ellsworth, W.L., 2000. A double-difference earthquake location algorithm: method and application to the Hayward fault. BSSA 90, 1353–1368.
Wessel, P., Smith, W.H., 1991. Free software helps maps and display data. EOS Trans. Am. Geophys. Union 72, 441.
Yamada, T., Mori, J.J., Ide, S., Kawakata, H., Iio, Y., Ogasawara, H., 2005. Radiation efficiency and apparent stress of small earthquakes in a South African gold mine. JGR 110. https://doi.org/10.1029/2004JB003221.
Zollo, A., Capuano, P., Singh, Sh.K., 1995. Use of small earthquake records to determine the source time functions of larger earthquakes: an alternative method and an application. BSSA 85 (4), 1249–1256.